

---

# Spherical Shock-Ignition Experiments with the 40 + 20-Beam Configuration on OMEGA

## Introduction

Shock ignition (SI)<sup>1</sup> is a promising new concept in direct-drive inertial confinement fusion (ICF) that achieves thermonuclear ignition and burn by a strong focusing shock wave in a pre-compressed DT shell.<sup>2</sup> Shock ignition, as described in Ref. 1, is a two-step scheme designed to enhance the hot-spot compression with respect to the single-step conventional hot-spot ignition.<sup>3</sup> SI uses a moderate-intensity assembly laser pulse followed by a subnanosecond high-intensity spike that launches a strong shock wave (the ignitor shock) into the imploding shell. It is important to emphasize that SI does not use a shock wave to directly ignite the dense fuel;<sup>4</sup> instead, it relies on the collision of the ignitor and the rebound shock waves at the inner shell surface to raise the hot-spot pressure.<sup>1</sup> A non-isobaric fuel assembly with a centrally peaked pressure profile makes SI more energy efficient by lowering the ignition threshold compared to isobaric assemblies.<sup>1</sup> Thick-shell targets containing more fuel can be compressed on a low adiabat with a low implosion velocity, which promises high fusion gains<sup>1,2,5-7</sup> at moderate laser energies. One-dimensional (1-D) simulations<sup>7,8</sup> have described igniting SI designs with as low as ~300 kJ of total laser energy. The SI requirements for laser pulse shaping are more demanding than in conventional hot-spot-ignition designs but are still within the pulse-shaping capabilities of currently operating laser systems like the National Ignition Facility (NIF).<sup>9</sup> Proof-of-principle experiments on the NIF were recently proposed;<sup>10</sup> also, SI is considered to be a viable option<sup>8</sup> for the European direct-drive HiPER project.<sup>11</sup>

The intensity of the spike pulse is expected to be a few times of  $10^{15}$  W/cm<sup>2</sup>. At these high intensities, parametric plasma instabilities<sup>12</sup> such as stimulated Brillouin scattering (SBS), stimulated Raman scattering (SRS), and the two-plasmon-decay (TPD) instability are of concern in an ignition target design for two reasons: The instabilities generate energetic electrons that might preheat the shell with the consequence of reducing the final core compression and they increase the back-reflection of the laser light from the target, degrading the laser-energy coupling to the capsule. SI designs typically apply lower laser intensity during the main part of the drive than in

hot-spot designs, so these issues might be less important during the early compression phase. Strong growth of laser-plasma instabilities and significant transfer of laser energy to hot electrons are expected during the high-intensity ignitor spike. The areal density increases during the implosion, and if the range of the hot electrons is less than the shell thickness, the electrons are stopped in the outer regions of the shell and do not considerably increase the adiabat of the inner part of the shell.<sup>13</sup> The hot electrons might then be advantageous for SI because they improve the shock strength. The effect of hot electrons on a NIF-scale SI target<sup>13</sup> was modeled in 1-D for a marginal igniting target using a multigroup diffusion model<sup>14</sup> for the hot electrons. The ignition (time) window for shock launching is considerably wider when the effects of moderate-energy hot electrons are included. The simulations<sup>13</sup> show that a NIF-scale target can efficiently stop up to 150-keV electrons that are generated during the spike pulse. Hot electrons can be beneficial for SI as long as their range is shorter than the shell's thickness. Important parameters are therefore the hot-electron temperature, the amount of laser energy that is transferred into electrons, and the time of generation.

This article presents SI experiments on the OMEGA laser<sup>15</sup> that use a novel beam configuration called the 40 + 20-beam configuration. Preliminary results with this configuration are discussed in Ref. 16. It uses 40 of the 60 OMEGA beams to implode the target with a low-intensity laser pulse, and the remaining 20 beams are tightly focused to launch a late shock into the imploding shell. Compared to the highly symmetric 60-beam implosions, irradiation nonuniformity with normal-incidence beams is higher in the 40 + 20 configuration. The implosion performance was also studied with a beam configuration with repointed beams. The experiments demonstrated significant improvement in implosion performance (higher neutron yield, higher areal density, and rounder core in x-ray images) with repointed beams. Two-dimensional (2-D) hydrodynamic simulations were performed for the repointed beam configuration. A similar concept, using a dedicated group of beams with a low-intensity pulse to implode the capsule and a second group of beams with a short high-intensity pulse for the

ignitor shock wave, might be implemented on the NIF.<sup>17</sup> The 40 + 20 configuration makes it possible to study high-intensity coupling on OMEGA and to measure hot-electron production and laser backscattering for intensities that are SI relevant. Previous spherical target SI experiments<sup>18</sup> on OMEGA studied the fuel assembly with 60-beam symmetric implosions. In those experiments, the shock wave was launched by a spike at the end of the pulse on all 60 beams with a maximum intensity of  $\sim 7 \times 10^{14}$  W/cm<sup>2</sup>. OMEGA cannot produce the requisite SI intensity with a compression pulse using the symmetric 60-beam configuration on a standard target because it leads to intensities that are too low to study laser–plasma instabilities. Switching to the 40 + 20-beam configuration allows one to use two separate pulse shapes with high-intensity beams tightly focused to reach intensities up to  $\sim 8 \times 10^{15}$  W/cm<sup>2</sup>. While the surface-averaged intensity is still rather low ( $\sim 9 \times 10^{14}$  W/cm<sup>2</sup>), the single-beam intensities are sufficiently high to study laser–plasma interactions at shock-ignition–relevant intensities. The objectives of this work are to study the implosion performance in the 40 + 20-beam configuration, the coupling of laser energy from high-intensity beams into a spherically imploding capsule, and the laser–plasma instabilities at SI-relevant laser intensities.

This article is organized as follows: the beam configurations are presented; the targets, laser pulse shapes, and diagnostics are described; the areal-density measurements and neutron measurements, including 2-D hydrodynamic simulations, are discussed; and the time-resolved hard x-ray and laser backscatter measurements are presented.

### Beam Configurations

OMEGA is a 60-beam laser that was built for direct-drive experiments operating at the third harmonic ( $\lambda = 351$  nm) of the Nd:glass laser wavelength. The 60 beams are symmetrically distributed around the target chamber in a soccer-ball geometry with the beams located at the vertices of hexagons and pentagons. OMEGA consists of three laser legs, each feeding two clusters with ten beams per cluster; leg 1 feeds clusters 1 and 4, leg 2 feeds clusters 2 and 5, and leg 3 feeds clusters 3 and 6. It is possible to use two independent pulse shapes: one pulse shape in one of the legs and the other pulse shape in the other two legs. For SI studies with a spherical target, this opens up the opportunity to use two separate pulse shapes with independent control over the two beam groups. One pulse shape in two legs implodes the capsule and a short high-intensity spike pulse in the third leg drives a late shock. Two different beam-pointing configurations were used; they are designated A and B in the following configurations. Configuration A used clusters 1, 3, 4, and 6 for the drive and clusters 2 and 5 for the

spike with all beams pointed to target center. The configuration with this particular choice of clusters resulted in significant target illumination nonuniformity because of the spatial and temporal separation between both beam groups. The pattern of the 40 drive beams is not as regular as in a standard 60-beam implosion, and, assuming perfect power balance, the irradiation nonuniformity was calculated to be  $\sim 11\%$  root-mean-square (rms) variation compared to less than  $\sim 1\%$  in a standard 60-beam spherically symmetric case.<sup>19</sup> A beam profile with a super-Gaussian shape given by  $I(r_\mu) = I_0 \exp[-(r_\mu/352)^{4.1}]$  (where  $r_\mu$  is the radius in microns) was assumed in the 40 drive beams. The focal spot for the 40 drive beams is obtained with distributed phase plates<sup>20</sup> with a super-Gaussian intensity distribution of fourth order, and the laser light was smoothed with polarization smoothing.<sup>21</sup> In configuration B, clusters 1, 2, 4, and 5 were used for the drive and clusters 3 and 6 for the spike. The irradiation nonuniformity in the 40 drive beams was  $\sim 7\%$  rms in this configuration, which was lower than in the previous configuration. It was further improved to  $\sim 3\%$  rms by repointing the beams. Most of the 40 drive beams were moved individually, as shown in Fig. 130.66, with the arrows representing direction and amount of shift for each beam.

Original beam positions and displacements

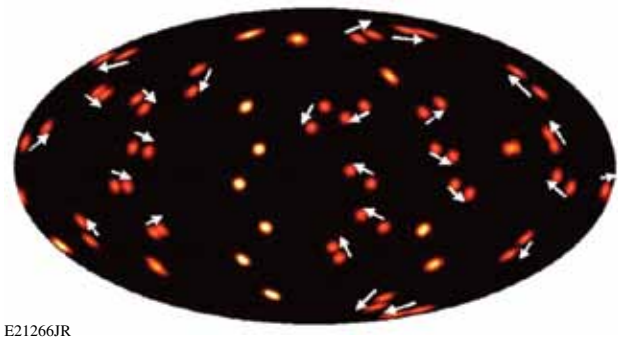


Figure 130.66

Aitoff representation of the original beam positions and repositioned positions of the 40 drive beams. Arrows indicate the direction and amount of displacement. Some beams were not moved. The configuration with repositioned beams is referred to as configuration B, while in configuration A all beams are pointed to target center.

Figure 130.67 shows the intensity variation of the 40 repositioned drive beams in (a) an Aitoff presentation and (b) a 3-D rendering. The illumination pattern in Fig. 130.67(b) was averaged over the azimuthal angle, which resulted in the axisymmetric illumination pattern shown in Fig. 130.67(c) that was used as input in 2-D cylindrical symmetric simulations with the radiation–hydrodynamic code CHIC.<sup>22</sup> Figure 130.68 shows the laser-intensity variation of the axisymmetric irradiation

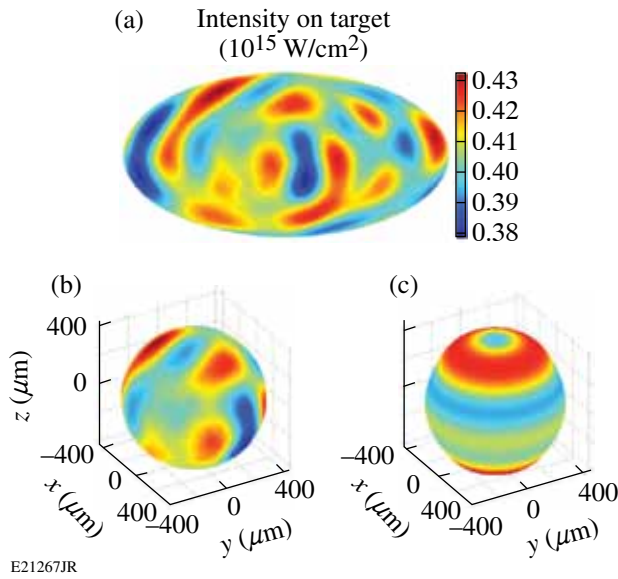


Figure 130.67 Intensity variation of 40 repointed drive beams (configuration B) in (a) an Aitoff representation and (b) a 3-D rendering. (c) The azimuthally averaged intensity distribution was used as input in 2-D cylindrical symmetric hydrodynamic simulations with the code CHIC.<sup>22</sup>

tion pattern versus polar angle and a Legendre-mode analysis, indicating that the modes  $\ell = 2, 4, 6,$  and  $7$  are dominant. In addition, a robustness study with respect to power imbalance was performed. A power imbalance of about  $\pm 8\%$  on the illumination was assumed. From six random power configurations, the results show that the nonuniformity increases by  $\sim 25\%$  to  $\sim 3.5\%$  rms. Besides the Legendre mode  $\ell = 2$ , the odd modes 1 and 3 are considerably increased in the presence of power imbalance. Moreover, the maximum of the  $\ell = 1$  amplitude is equivalent to a target offset of  $5 \mu\text{m}$ , which further indicates that the 40-beam configuration is sensitive to power imbalance.

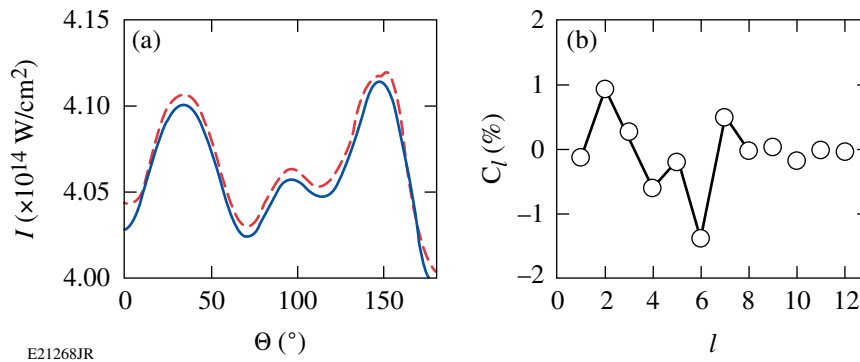


Figure 130.68 Laser-intensity variation on target of the axisymmetric irradiation pattern from Fig. 130.67(c) as a function of (a) polar angle (solid curve—initial irradiation; dashed curve—Legendre polynomial representation) and (b) Legendre-mode analysis of the pattern for  $\ell$  below 12. Dominant modes are  $\ell = 2, 4, 6,$  and  $7$ .

To achieve best symmetry in configuration B, a beam repointing from target center was also performed for the 20 spike beams, as shown in Fig. 130.69. The 20 beams were moved to the vertices of a dodecahedron pattern. This means that the beams were repositioned on four rings at the following polar angles:  $37.4^\circ, 79.2^\circ, 100.8^\circ,$  and  $142.6^\circ$ . Figure 130.69 shows that each of the 20 spike beams was moved individually, where the arrows represent the direction and the amount of shift of each beam. Significantly larger shifts were used in the 20 spike beams.

The single-beam laser intensity of the 20 spike beams on target was controlled by changing the radial beam's focal position. It is important to make a clear distinction between the average intensity  $\langle I_{\text{spike}} \rangle$  and the single-beam intensity (SBI) of the spike beams on the capsule surface. The SBI ranges from  $I_{\text{spike}} \sim 0.5 \times 10^{15}$  to  $\sim 8 \times 10^{15} \text{ W/cm}^2$ , while the average intensity on target is not affected as much by the focusing and is  $\langle I_{\text{spike}} \rangle \sim 0.5 \times 10^{15} \text{ W/cm}^2$ . The average intensity is the relevant quantity to determine the shock strength and the

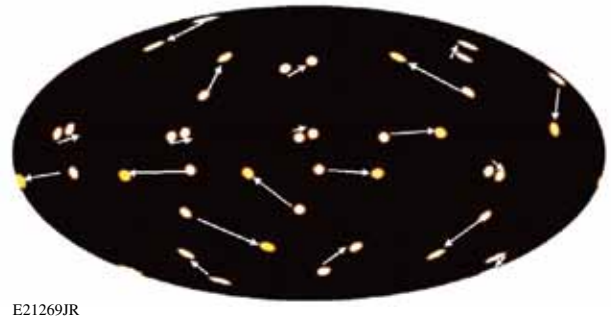


Figure 130.69 Aitoff representation of the original beam positions and repositioned positions of the 20 spike beams. Arrows indicate the direction and amount of displacement.

equivalent pressure from the spike beams. The nominal single-beam laser intensity is quoted for vacuum at the location of the critical-density plasma surface at the time when the spike pulse was launched during the implosion as calculated by simulations with the radiation-hydrodynamic codes *LILAC*<sup>14</sup> and *CHIC*. The distance from the critical-density surface to the capsule center was  $\sim 0.3$  mm at 2.7 ns. At best focus, the diameter of the spike beams was estimated with  $\sim 80$   $\mu\text{m}$ , which gave an SBI of  $\sim 8 \times 10^{15}$   $\text{W}/\text{cm}^2$  in vacuum. The actual intensity might be different as a result of plasma effects. Figure 130.70 shows the intensity pattern of the 20 spike beams for the following spot sizes:  $\sim 140$   $\mu\text{m}$  (SBI  $\sim 2.5 \times 10^{15}$   $\text{W}/\text{cm}^2$ ),  $\sim 220$   $\mu\text{m}$  (SBI  $\sim$

$1 \times 10^{15}$   $\text{W}/\text{cm}^2$ ), and  $\sim 580$   $\mu\text{m}$  (SBI  $\sim 0.5 \times 10^{15}$   $\text{W}/\text{cm}^2$ ) without the drive beams. The foci of the 20 spike beams did not overlap at the critical-density surface for most lens positions. Only at the lowest intensity for an  $\sim 580$ - $\mu\text{m}$  spot size did the beams partially overlapped. This created local peak intensities of  $\sim 0.7 \times 10^{15}$   $\text{W}/\text{cm}^2$  in some regions where several beams overlapped. Except for some shots with small-spot phase plates,<sup>23</sup> phase plates were not used in the spike beams for most of the shots.

### Targets, Pulse Shapes, and Diagnostics

The targets were  $\sim 34$ - to  $36$ - $\mu\text{m}$ -thick,  $\sim 430$ - $\mu\text{m}$ -outer-radius, deuterated plastic shells coated outside with a  $0.1$ - $\mu\text{m}$  layer of aluminum. They were filled with  $\text{D}_2$  gas at a pressure of  $\sim 25$  atm. The capsules were imploded on a low adiabat ( $\alpha \sim 2.4$ ) with a drive pulse shape that is shown for a single beam by the solid curve in Fig. 130.71. The adiabat  $\alpha$  is defined as the ratio of the plasma pressure to the Fermi pressure of a degenerate electron gas. The pulse shape contained  $\sim 14$  kJ of laser energy in 40 beams. Standard 60-beam implosions with the same pulse shape and similar targets, but higher drive energy, are discussed in Refs. 18 and 24. The drive pulse consists of an  $\sim 100$ -ps full-width-at-half-maximum (FWHM) picket pulse preceding a shaped main drive portion with a total duration of 2.7 ns. The 20 spike beams delivered a total energy of  $\sim 5$  kJ on target and used an  $\sim 600$ -ps FWHM square pulse (dashed curve in Fig. 130.71).

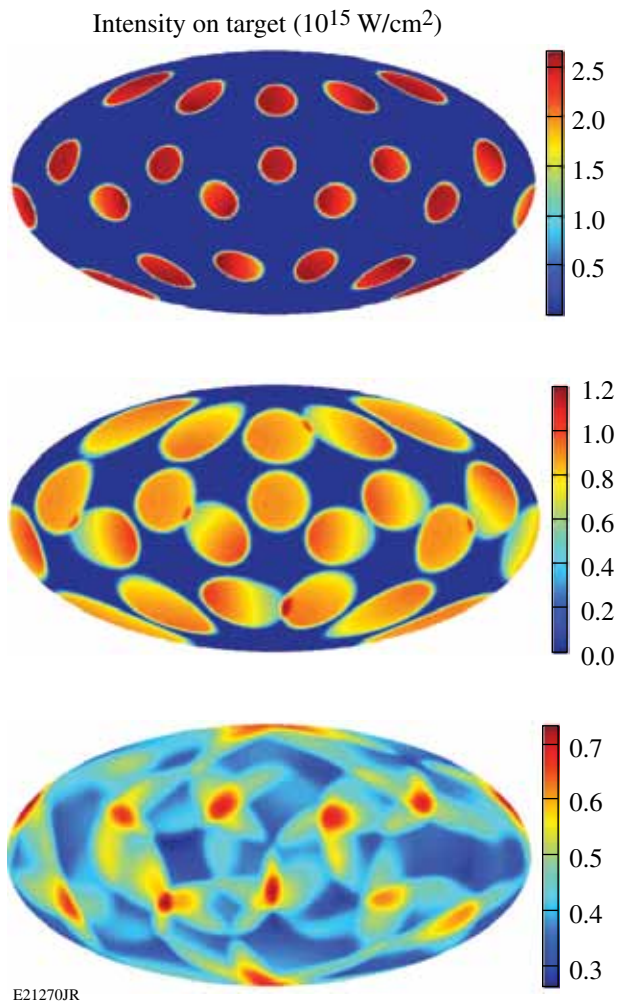


Figure 130.70 Intensity variations of the 20 repointed spike beams (configuration B), on the dodecahedron vertices in an Aitoff representation. Different lens defocus positions resulted in single-beam spike intensities of  $\sim 2.5 \times 10^{15}$   $\text{W}/\text{cm}^2$ ,  $\sim 1 \times 10^{15}$   $\text{W}/\text{cm}^2$ , and  $\sim 0.5 \times 10^{15}$   $\text{W}/\text{cm}^2$ , respectively (from top to bottom).

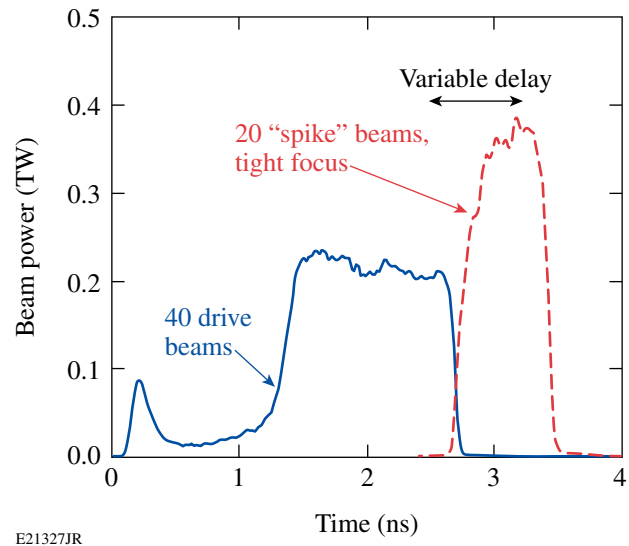


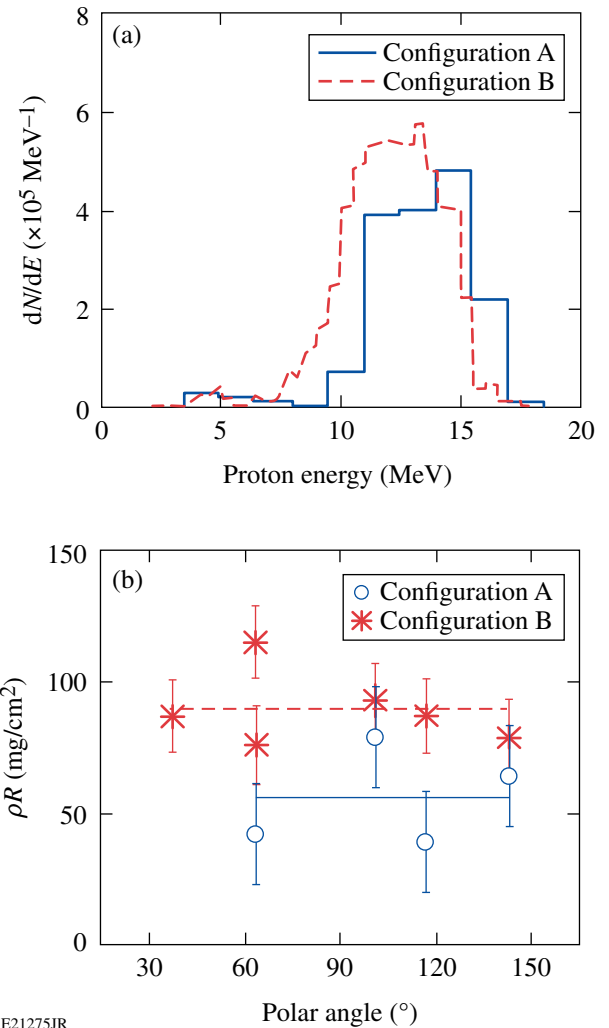
Figure 130.71 Single-beam power versus time of the drive-pulse shape (solid) for the 40 beams and the high-intensity pulse (dashed) for the 20 spike beams. Beam delay and spike intensity were varied.

The experimental observables were the spatially resolved x-ray emission from pinhole cameras,<sup>25</sup> the neutron yield,<sup>26</sup> the neutron-rate,<sup>27</sup> the backscattered laser energy,<sup>28</sup> the hard x-ray signal,<sup>29</sup> and the neutron-rate-averaged areal density ( $\rho R$ ).<sup>30</sup> The laser light reflected back from the imploded capsule was measured from two adjacent beam ports (a spike-beam and a drive-beam port), which were equipped with a full-aperture backscatter station (FABS).<sup>28</sup> Time-resolved spectra were recorded by two streaked spectrometers covering the wavelength ranges of  $351 \pm 3$  nm for SBS and 450 to 700 nm for SRS. The total backscattered energy in either of these spectral ranges was measured by calorimeters with an uncertainty of  $\pm 10\%$ . The hard x-ray (HXR) signals were measured with  $\sim 100$ -ps temporal resolution by the HXR detector with four channels measuring x rays  $>20$ ,  $>40$ ,  $>60$ , and  $>80$  keV, respectively.<sup>29</sup> The HXR measurements were used to infer the hot-electron temperature.<sup>29</sup>

### Areal-Density Measurements and CHIC Simulations

Close to stagnation of the imploded shell, secondary deuterium fusion reactions in the central hot-spot region produce protons that pass through the dense, cold shell, where they lose energy. Measurement of the downshifted kinetic-energy spectrum provides information about the shell's areal density. This technique makes it possible to accurately reconstruct the proton spectrum and to infer  $\rho R$ , as discussed in detail in Ref. 30. Figure 130.72(a) shows two spectra taken at an SBI of  $\sim 3 \times 10^{15}$  W/cm<sup>2</sup>. Each spectrum represents the average over several spectra from various lines of sight. The solid histogram is from an implosion with configuration A and the dashed histogram is from configuration B. Lower proton energy indicates a higher  $\rho R$ . The corresponding  $\rho R$  from the different lines of sight versus the target chamber polar angle is plotted in Fig. 130.72(b) with cross and circle symbols. The corresponding lines represent the average value. The  $\rho R$  is almost a factor of 2 higher with configuration B, showing that repointing the beams significantly improved the implosion performance. The  $\rho R$  varies with the observation direction, indicating considerable modulation in  $\rho R$ , which is primarily due to illumination nonuniformities.

Two-dimensional simulations with the code CHIC studied the density and temperature modulations of the imploded capsule at stagnation for configuration B [see Fig. 130.73(a)]. Figure 130.73(b) shows simulated (curves) and measured (circles) areal density as a function of the polar angle. The black solid curve is from the 2-D simulation while the dashed line is from a 1-D simulation. The squares mark the 2-D-simulated values at those polar angles used in the measurement. The



E21275JR

Figure 130.72

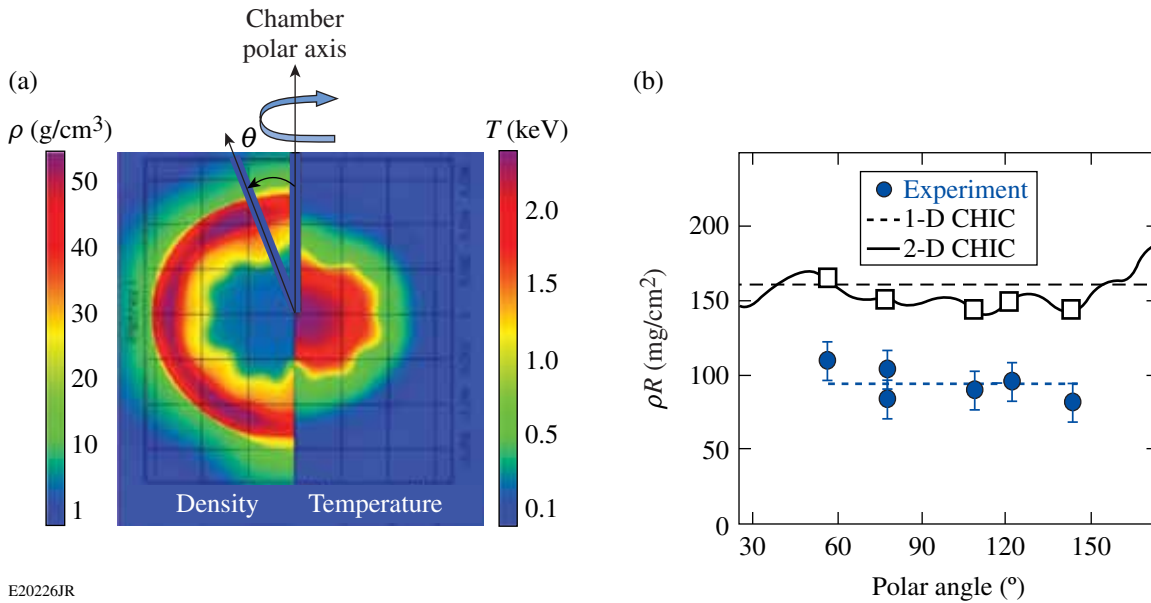
(a) Secondary proton spectra from an implosion with beam configuration A (solid) and for configuration B (dashed) under similar conditions with SBI  $\sim 3 \times 10^{15}$  W/cm<sup>2</sup> and spike onset at  $\sim 2.3$  ns. A lower proton energy spectrum indicates higher areal density. (b) Corresponding neutron-rate-averaged areal densities from different lines of sight are plotted versus the target chamber polar angle.

dotted line is the averaged experimental value. Note that the simulation values are higher because they represent  $\rho R$  at peak neutron production, while the experimental values are temporally averaged over the neutron-production rate.

The  $\rho R$  was measured for various onsets of the spike beams with respect to the start of the drive pulse and various SBI. The spike onset was varied from 2.1 to 2.8 ns (see Fig. 130.71). Figure 130.74 shows the measured angular-averaged  $\rho R$ . The symbols represent 40 + 20 implosions, and the line in Fig. 130.74(b) represents a 40-beam implosion with no spike and  $\sim 14$  kJ of

energy. In configuration A [Fig. 130.74(a)], the proton yield from implosions with only 40 beams was too low to provide a  $\rho R$  measurement. The  $\rho R$  values are consistently higher in configuration B [see Fig. 130.74(b)], showing improved implosion

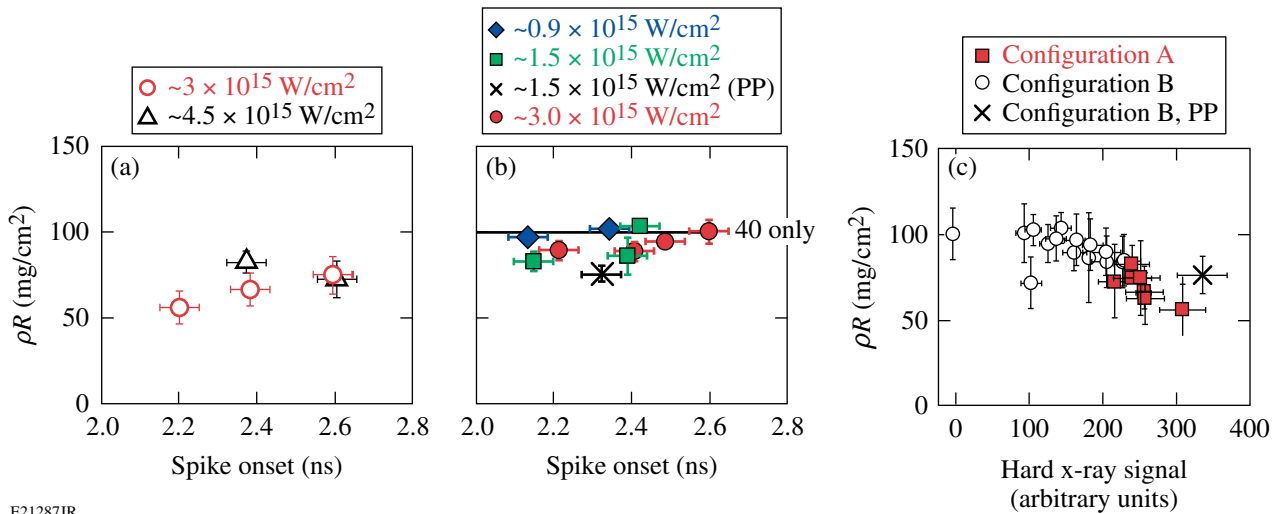
performance. For  $SBI > 1.5 \times 10^{15} \text{ W/cm}^2$  there is a tendency of lower  $\rho R$  for early spike onset. The lower  $\rho R$  is correlated with a higher hard x-ray signal [see Fig. 130.74(c)], which could indicate preheating by hot electrons.



E20226JR

Figure 130.73

Two-dimensional (2-D) CHIC<sup>22</sup> simulations show significant modulations in the compressed shell. (a) Simulated density and temperature map of a 40 + 20-beam implosion close to stagnation. (b) Simulated (solid and dashed curves, squares) and measured areal density (circles) as functions of the polar angle. The SBI was  $\sim 3 \times 10^{15} \text{ W/cm}^2$  and spike onset was at  $\sim 2.6 \text{ ns}$ .



E21287JR

Figure 130.74

Measured areal densities from 40 + 20 implosions for (a) configuration A, (b) configuration B, and (c) both configurations versus the measured hard x-ray signal. The solid line in (b) represents the measured areal density of a 40-beam implosion. The spike onset and SBI were varied. The solid squares and open circles in (c) represent the measurements in configurations A and B, respectively, and  $\times$  represents the measurement with phase plates in the spike beams in configuration B.

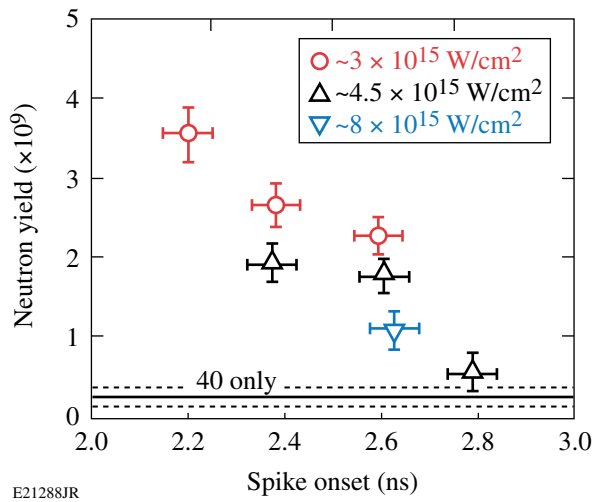


Figure 130.75

Measured neutron yield in 40 + 20-beam implosions for various spike-onset times and single-beam intensities for configuration A.

### Neutron Measurements and CHIC Simulations

Figure 130.75 shows the measured neutron yield for beam configuration A for various spike-onset times and single-beam intensities. A maximum yield of  $\sim 3.5 \times 10^9$  was measured for the shortest time delay. Two reference implosions with only the 40 drive beams produced neutron yields of  $1.4 \times 10^8$  and  $3.7 \times 10^8$ ; the solid line in Fig. 130.75 represents the average of those yields. The low yield of the 40-beam implosion is caused by the large illumination nonuniformity in configuration A, which was also seen in a strongly perturbed core in x-ray pinhole camera images. The x-ray images<sup>25</sup> from two different views are shown in Fig. 130.76(a). The recorded x-ray emission is from the 2- to 7-keV range and comes from the outer-shell region, the target stalk, and the core region. Adding the spike beams mitigated the nonuniformities, leading to less core distortions [Fig. 130.76(b)] and an  $\sim 14\times$  increase in neutron yield for the shortest spike onset. This shows that a significant amount of the energy from the high-intensity beams was coupled into the capsule. The large illumination nonuniformity in configuration A was partially mitigated by the spike beams, which led to the recovery of the neutron yield. At high intensities, the experimental yield may be affected by a high plasma reflectivity (see **Backscatter Measurements**, p. 124), which lowers the coupling efficiency. With later spike onset, there was less temporal overlap between the drive and the spike pulse and a lower neutron signal was measured. The drive and spike pulses were completely separated at 2.8 ns, which is when the lowest neutron yield was measured in the 40 + 20 implosions. For configuration A, neutron yields were strongly affected by 3-D effects in a highly perturbed core.

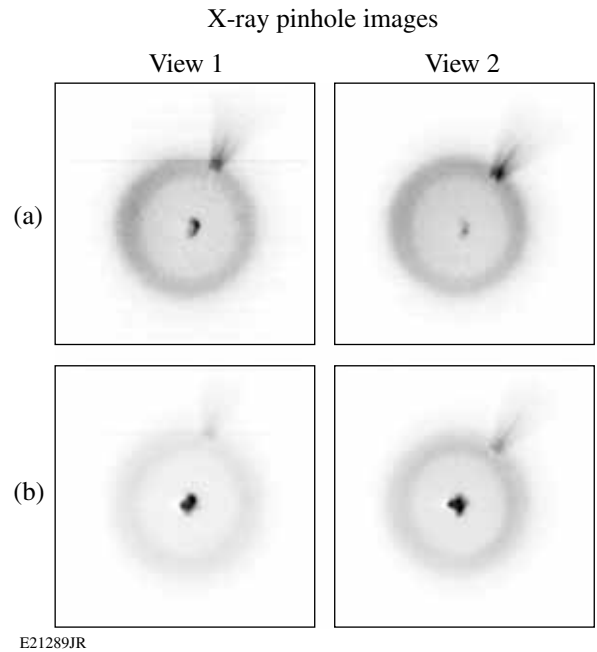


Figure 130.76

Measured time-integrated x-ray pinhole images for configuration A. Two views from different directions are shown in each row. (a) The top row represents a 40-beam implosion and (b) the lower row a 40 + 20 implosion. The V-shaped feature in the top right is the emission from the target stalk.

Similar implosions were performed with configuration B, where the illumination uniformity was significantly improved. This was demonstrated by a much rounder core in the x-ray pinhole camera images [compare Fig. 130.77(a) to Fig. 130.76(a)]. Adding the 20 spike beams did not further improve the roundness of the core emission. Figures 130.77(b) and 130.77(c) show corresponding images using (b) no phase plates and (c) small spot phase plates in the 20 spike beams, respectively. Core distortions are even slightly worse than in Fig. 130.77(a). A stronger x-ray emission is observed in Fig. 130.77(c) with phase plates. Figure 130.78 shows the (a) measured and (b) simulated neutron yields for these implosions. Implosions with repointed 40 drive beams produced neutron yields of  $\sim 1.5 \times 10^9$  [solid line in Fig. 130.78(a)], which is a factor of  $\sim 6$  higher than in the implosions where beams were pointed to target center. Adding the 20 spike beams, and therefore more energy on target, enhances the yield further by a factor of up to 2.3, with a trend of slightly lower yields at longer times. With 20 spike beams, the overall neutron yield is very similar to configuration A. The neutron yield shows no significant dependence on the spike intensity. A similar trend is observed in the predicted neutron yield from 1-D CHIC simulations [Fig. 130.78(b)]. There the enhancement is up to a factor of  $\sim 3.5$  when the spike beams are added, slightly more than what was measured. Configuration B

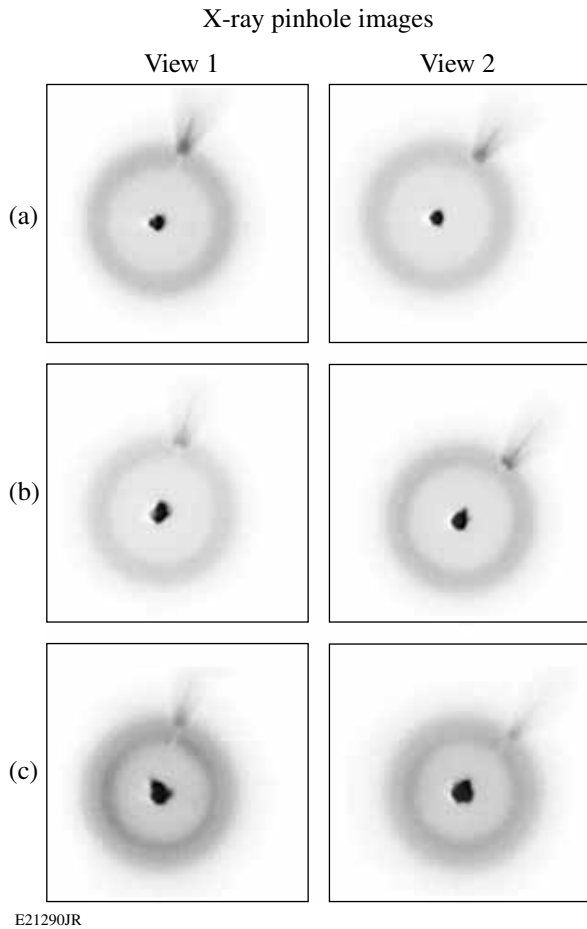


Figure 130.77

Measured time-integrated x-ray pinhole images for configuration B. Two views from different directions are shown in each row. (a) The top row represents a 40-beam implosion, (b) the middle row a 40 + 20 implosion (no phase plates in the spike beams), and (c) the lower row a 40 + 20 implosion with phase plates in the spike beams.

starts with a good illumination pattern in the 40 drive beams, but the 20 spike beams probably increased nonuniformities, which is seen in the x-ray pinhole images in Figs. 130.77(b) and 130.77(c). This might explain why the yield increase is less than predicted. The yield-over-clean (YOC) ratio, defined as the measured-to-predicted neutron number, is 3% to 5% for these experiments. The low YOC can be explained by a strong Rayleigh–Taylor instability growth during the acceleration phase in these low-velocity plastic-shell implosions and a substantial shell–fuel mixing that quenches fusion reactions.<sup>18</sup>

The neutron temporal diagnostic<sup>27</sup> recorded the fusion reaction-rate history in most of the implosions, provided that the neutron yield was above  $\sim 1 \times 10^9$ . The signals were noisy and the peak of the measured neutron rate or “bang time” was

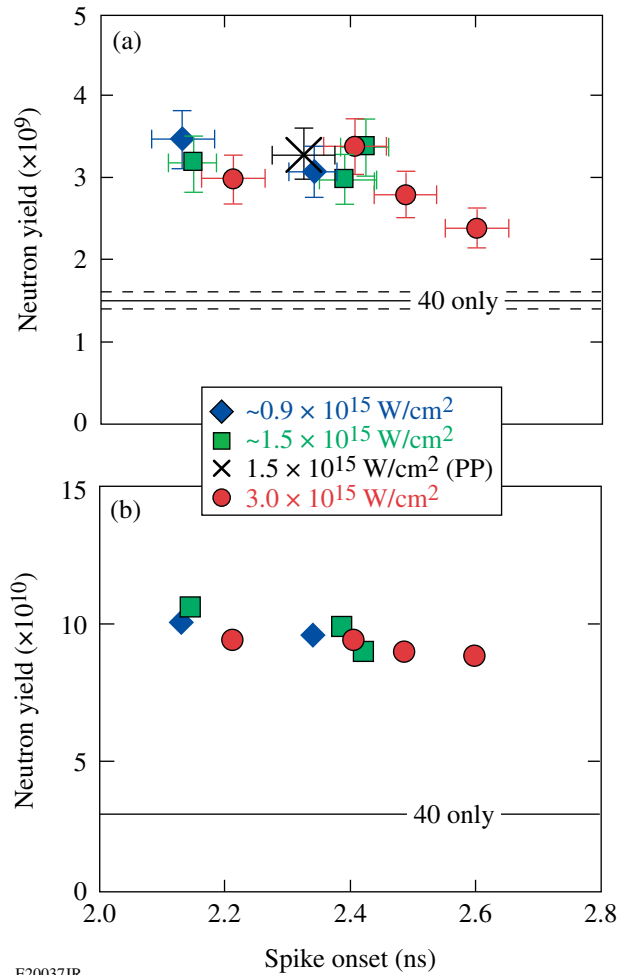


Figure 130.78

(a) Measured and (b) 1-D-simulated neutron yields for configuration B.

obtained by fitting a Gaussian curve to the signals. The error in determining the bang time is estimated with  $\sim 50$  ps. The bang time versus spike onset is plotted in Fig. 130.79(a). Bang times are earlier in configuration A for a given spike onset. The general trend for both data sets is that the bang time is later with a later onset of the spike pulse. The gray band marks the range of measured bang times from 40 drive beam implosions in configuration B. The solid line is a linear fit through the squares. The slope of this line is  $\sim 1.6\times$  larger than the slope of the dashed line, which is a linear fit through the circles. This indicates a stronger effect of the spike pulse in configuration A. However, the earliest bang time ( $\sim 3.59$  ns) was measured in one 40 + 20 shot with phase plates in the spike beams and in configuration B. This is  $\sim 200$  ps earlier than in the 40-drive-beam implosions. Figure 130.79(b) shows that it is not so much the particular beam configuration that is important for the bang time; the amount of hot electrons that are generated (see **Hard**

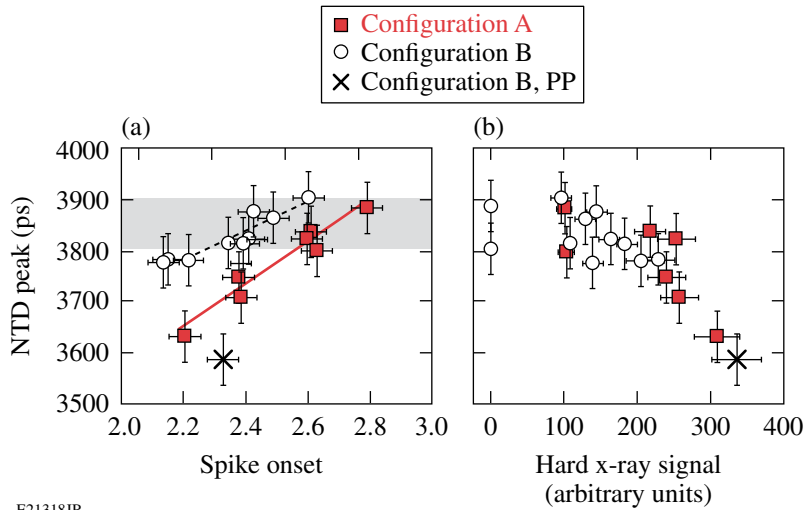


Figure 130.79 Measured neutron bang time versus (a) the spike onset time and (b) the hard x-ray signal. The solid squares and open circles represent the measurements in configurations A and B, respectively, and × represents the measurement with phase plates in the spike beams in configuration B. The gray band in (a) denotes the range of measured bang times in 40-beam implosions.

E21318JR

**X-Ray Measurements**, p. 122) is more important. A clear correlation of the bang time with the measured hard x-ray signal is observed. An earlier bang time correlates with a higher x-ray signal, indicating that the hot electrons responsible for the hard x-ray emission affect the hydrodynamic implosion.

Figure 130.80 shows electron-temperature and pressure maps obtained from various 2-D CHIC simulations for configuration B. Hot electrons were not included in the simulations. This is probably justified for most of the shots in configuration B without phase plates since those shots are less affected by hot electrons (see Fig. 130.79). Figure 130.80(a) shows the case without a spike pulse. The 40-beam illumination corresponds to that rendered in Fig. 130.67(c). In this case the corona temperature and pressure are isotropic during the shell implosion, and the shock pressure is about 50 Mbar at the end of the drive pulse ( $t = 2.6$  ns). Figures 130.80(b)–130.80(d) show 2-D simulations 300 ps after the spike onset for different focusing conditions of

the spike beams (see Fig. 130.70), i.e., with different SBI. The temperature in Fig. 130.80(d) shows weak laser imprint in the corona from the spike illumination pattern, while with lower intensity the temperature becomes more symmetric because of a better spatial overlap of the 20 spike beams. Independent of the spike intensity on target, however, the pressure remains fairly symmetric with the same value of  $\sim 75$  Mbar. Some slight pressure modulations are observed at the highest intensity. The simulations show that the temperature in the conduction layer is always symmetric, which explains why the spike pressure keeps the same values in all the cases. For all focus conditions, the equivalent pressure can be estimated from the average spike intensity, which is  $\langle I_{\text{spike}} \rangle \sim 0.5 \times 10^{15}$  W/cm<sup>2</sup>. The total intensity on target is the sum of the spike intensity and the compression intensity ( $I_{\text{comp}} = \sim 0.4 \times 10^{15}$  W/cm<sup>2</sup>). For a laser absorption of about 70%, the absorbed intensity is

$$I_{\text{abs}} = \sim 0.7(I_{\text{comp}} + \langle I_{\text{spike}} \rangle) = \sim 0.6 \times 10^{15} \text{ W/cm}^2,$$

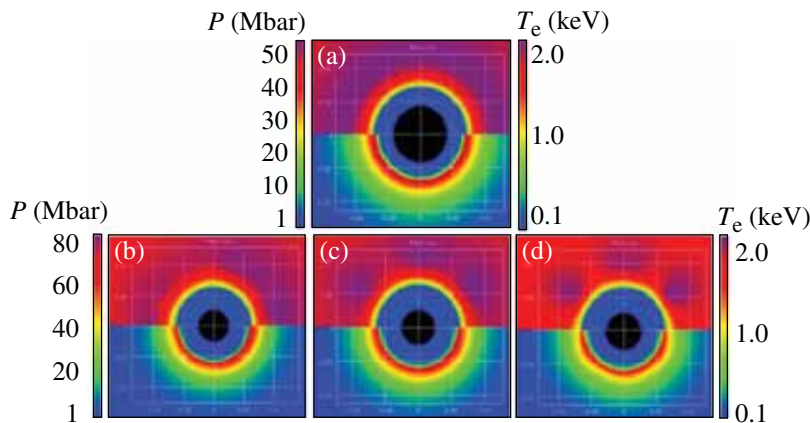


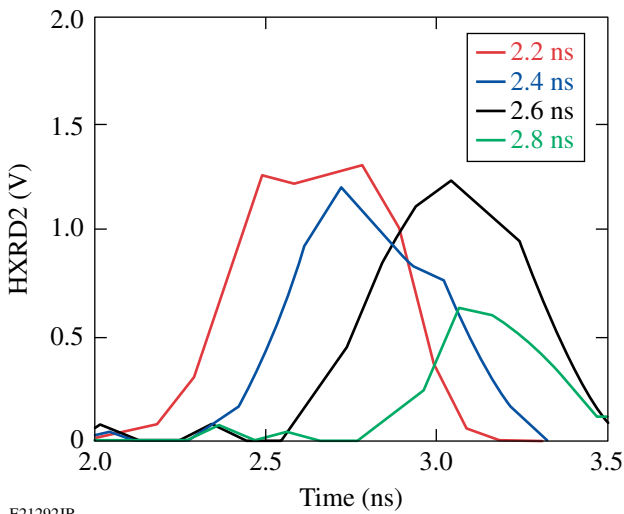
Figure 130.80 Two-dimensional CHIC simulations. Electron temperature (top half) and pressure (bottom half): (a) without a spike at the end of the drive pulse (2.6 ns) and with a spike, 300 ps after the spike onset (2.9 ns) with (b) SBI =  $0.5 \times 10^{15}$  W/cm<sup>2</sup>, (c) SBI =  $1 \times 10^{15}$  W/cm<sup>2</sup>, and (d) SBI =  $2.5 \times 10^{15}$  W/cm<sup>2</sup>. The temperature and pressure scales are the same for (b)–(d).

E21291JR

and the expected pressure is  $\sim 80$  Mbar for this intensity from a simple scaling law model,<sup>31</sup> in agreement with the simulated value. The 2-D simulations explain why for all SBI's, the spike pressure remains constant, as does, consequently, the neutron yield. This argument applies only for the experiments with configuration B, while for configuration A, the neutron yields are dominated by the illumination nonuniformities and their mitigation by the spike beams.

### Hard X-Ray Measurements

The hard x-ray (HXR) detector provides information on the temperature of the electron distribution. The measured time-resolved hard x-ray pulse from the  $>40$ -keV channel is shown in Fig. 130.81 for various spike-onset times. The hard x-ray pulse correlates with the spike laser pulse, with respect to both the onset and its duration. The hard x rays and, therefore, the hot electrons are predominantly produced by the high-intensity laser spike and are negligible when only the 40 low-intensity drive beams are used.

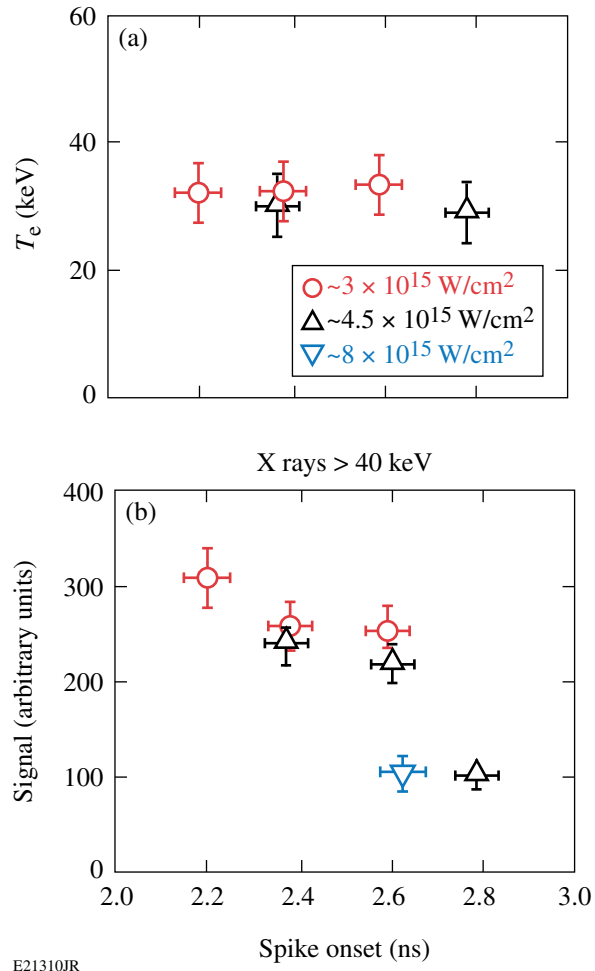


E21292JR

Figure 130.81

Measured time-resolved hard x-ray pulses for energies  $>40$  keV. The times in the legend indicate the onset of the spike pulse. The hard x-ray pulse is clearly correlated with the spike pulse, in both onset and duration.

The hot-electron temperature for configuration A [Fig. 130.82(a)] was determined by fitting estimated values from the convolution of an exponentially decaying hard x-ray spectrum with the sensitivity of the different channels of the HXR detector to the three measured higher-energy channels.<sup>29</sup> The lowest-energy channel was excluded from the fit. A hot-electron-energy distribution with a temperature of  $\sim 30$  keV was measured, independent of laser intensity and timing. Large-scale, collisional, 1-D particle-in-cell (PIC) simulations<sup>32</sup> for



E21310JR

Figure 130.82

(a) Inferred hot-electron temperature and (b) measured, time-integrated hard x-ray signal  $>40$  keV for configuration A.

laser intensities of  $10^{15}$  to  $10^{16}$   $W/cm^2$  using very similar plasma parameters, as in these experiments, reported hot-electron temperatures of  $\sim 25$  keV, with the primary source for hot electrons being SRS. Remarkably, the simulations<sup>32</sup> predict a relatively low, constant hot-electron temperature that will not change with laser intensity, in agreement with the experimental observation.

Figure 130.82(b) shows the time-integrated hard x-ray yield of the  $>40$ -keV channel. It is interesting to note that for implosions in configuration A, there is a clear correlation between the measured neutron signal (Fig. 130.75) and the hard x-ray signal [Fig. 130.82(b)], which suggests that the yield increase from adding the spike beams was partially due to hot electrons coupled into the outer regions of the compressing target. It can be excluded that hard x-ray interfered with the neutron-yield measurements because of proper shielding of the diagnostics and time-resolved measurements. Hard x-rays are measured

during the time of the spike pulse, while the neutron time-of-flight signal is measured much later in time. As mentioned before, the neutron signal is very sensitive to the condition of the target illumination. Adding the 20 spike beams in configuration A probably mitigated the nonuniformities, resulting in a much-higher ( $\times 14$ ) neutron yield when the 20 spike beams were added. This indicates that the spike beam's energy is partially coupled by hot electrons that slowed down in the dense shell.

Higher hard x-ray signals were measured for early spike onset, probably caused by a longer temporal overlap between drive and spike pulse, which suggests that electron plasma waves seeded by the drive pulse are amplified by the high-intensity spike. More overlap provides a longer time period when the electron-plasma waves are driven; therefore, more hot electrons and higher hard x-ray signals are generated. Hot-electron generation is caused by the SRS and TPD instabilities.<sup>33</sup> The foci of the 20 spike beams did not overlap at the critical density for those measurements, so effects from overlapping beams<sup>33</sup> are not expected and the hot-electron production is dominated by single-beam interactions with the target. At 2.6 ns, there are three shots with different intensities. The hard x-ray signal decreases with higher intensity. Two causes might explain this effect: First, the backscatter losses increase from  $\sim 10\%$  to  $\sim 35\%$  (see below) with higher intensity, reducing the coupling efficiency of the spike beams. Second, since the SBI was varied through the focus size while holding the energy constant, a higher intensity corresponds to a smaller spot size. This affects the total number of generated hot electrons and the hard x-ray signal. The number of hot electrons is proportional to the plasma volume intercepted by the high-intensity beams. When normalizing the measured hard x-ray signal by the estimated laser beam area at quarter-critical density, the

yield actually increases with laser intensity (see Fig. 130.83). This shows that the hot-electron production per area increases with laser intensity, presumably because of a larger growth of laser-plasma instabilities. As in previous experiments performed under similar conditions,<sup>33</sup> the hard x-ray signal saturates at intensities above  $\sim 2 \times 10^{15}$  W/cm<sup>2</sup>.

Similar measurements were performed for beam configuration B (see Fig. 130.84). Here, the SBI was varied between  $0.9 \times 10^{15}$  and  $\sim 3 \times 10^{15}$  W/cm<sup>2</sup>. In contrast to the previous experiment, the foci of the spike beams were large enough at the lowest intensity so that they partially overlapped [see Fig. 130.70(c)]. Not surprising, the lowest hard x-ray signal was measured for the lowest intensity. The inferred temperature was

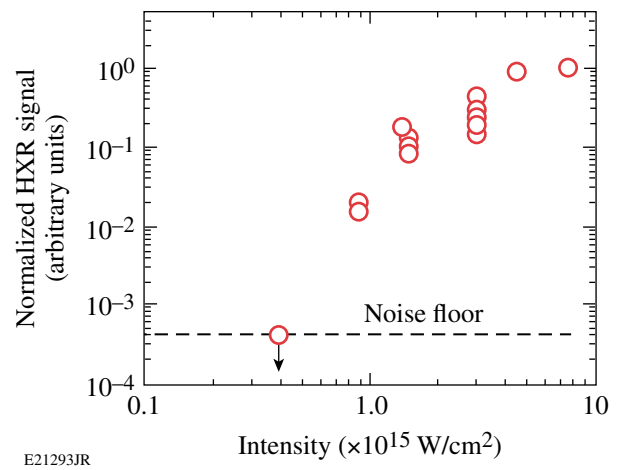


Figure 130.83  
Hard x-ray signal divided by the estimated laser-beam area at quarter-critical density as a function of SBI. The maximum signal was normalized to unity. Data from both configurations are plotted.

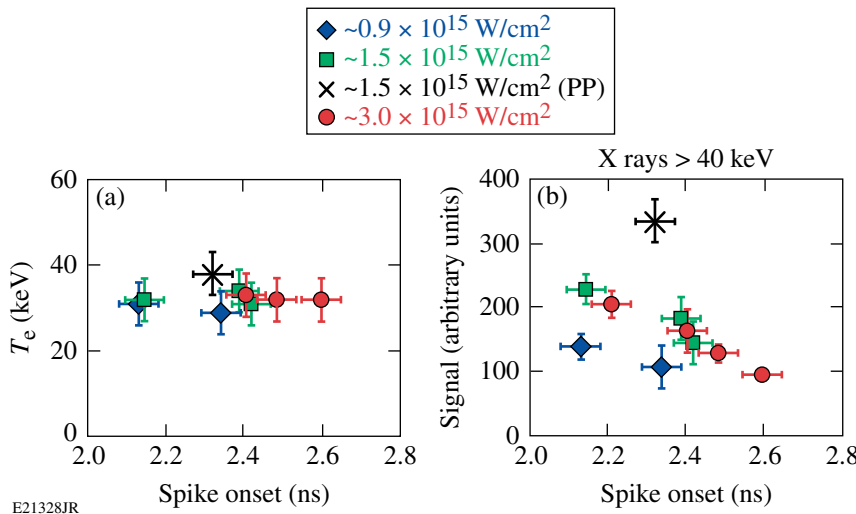


Figure 130.84  
(a) Inferred hot-electron temperature and (b) measured hard x-ray signal for configuration B.

~30 keV for all the shots without phase plates, independent of laser intensity and timing, which is very similar to the temperature in configuration A. A slightly higher temperature of ~40 keV was measured with phase plates, which also produced the highest hard x-ray signal for this beam configuration. Less backscattering (see **Backscatter Measurements** below) and less beam filamentation are expected with phase plates,<sup>34</sup> which should lead to higher laser intensity at quarter-critical density. It is expected that the laser-plasma instabilities are driven harder, which could then lead to a hotter electron population and more electrons. Only for this shot with phase plates, a measurable 3/2-harmonic signal<sup>33</sup> was present; the 3/2 signal was absent in all other shots without phase plates. The hotter electron distribution might therefore be caused by some contribution from TPD, while the shots without phase plates were dominated by SRS instability (see **Backscatter Measurements** below).

For beam configuration B, there is no clear correlation between the neutron signal [Fig. 130.78(a)] and hard x-ray signal [Fig. 130.84(b)]. This can be explained by the fact that in configuration B a relatively uniform 40-beam implosion is distorted when the 20 spike beams are added. The 20 spike beams impose a dodecahedron imprint pattern and seed modulations [see Fig. 130.80(d)] that increase the core deformation at peak compression (Fig. 130.73). Larger core distortions were also observed in x-ray pinhole images when the spike beams were added [Figs. 130.77(b) and 130.77(c)]. This led to more Rayleigh-Taylor instability growth and reduced the neutron yields despite the additional energy that was coupled into the imploding shell. In general, adding laser energy from the spike beams should help to compress the shell more and boost the neutron yield, but there is a trade-off between more energy coupled into the target and more seeds for instabilities.

### Backscatter Measurements

The plasma reflectivity was measured for various laser intensities. Figure 130.85 shows the percentage of back-reflected light in the (a) SRS and (b) SBS channels of one of the spike beams. The SRS signal increased in intensity by more than a factor of ~10 to up to 24% and dominated the backscattering at the highest intensity, while SBS increased moderately from ~5% to 12%. A very low level of SRS backscattering (~0.5%) was measured at  $\sim 1.5 \times 10^{15}$  W/cm<sup>2</sup> with phase plates in the spike beams. The simultaneously measured back-reflection through the neighboring drive-beam port, i.e., one of the 40 beam ports delivering the assembly pulse, was low and remained constant at the same level as in implosions without the 20 spike beams for all timings and intensities (see Fig. 130.86). In the drive beam, SRS stayed below 1% and SBS stayed in

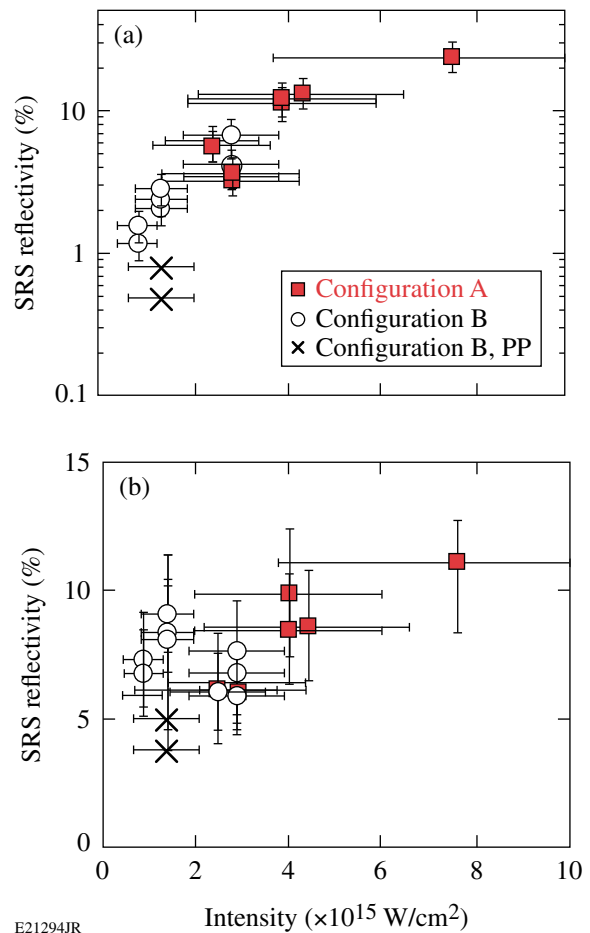


Figure 130.85

Percentage of back-reflected laser light in a spike beam port by (a) SRS and (b) SBS as a function of SBI. Most of the high-intensity shots were done with configuration A denoted by the full symbols. The open symbols represent reprinted beams (configuration B). The lowest reflectivity was measured with configuration B and phase plates (cross).

the 2% to 4% range. This shows that the light from the spike beams was scattered back in a narrow cone and did not spill over into adjacent ports.

It has been shown<sup>35,36</sup> that smoothing the intensity distribution in the focal spot with spatial, temporal, and polarization smoothing schemes can substantially reduce the backscattering. This is attributed to a reduction of filamentation.<sup>34</sup> In most of the shots, no phase plates were used in the spike beams, which could explain the high levels of backscattering. The sum of SBS and SRS backscatter was lowest (~6%) with phase plates, while without phase plates, the reflectivity increased from ~8% at  $\sim 0.9 \times 10^{15}$  W/cm<sup>2</sup> to ~36% at  $\sim 8 \times 10^{15}$  W/cm<sup>2</sup>. Most of the high-intensity shots were done with configuration A, but some shots were taken at  $3 \times 10^{15}$  W/cm<sup>2</sup> with both beam configurations. The backscatter was the same within the measurement

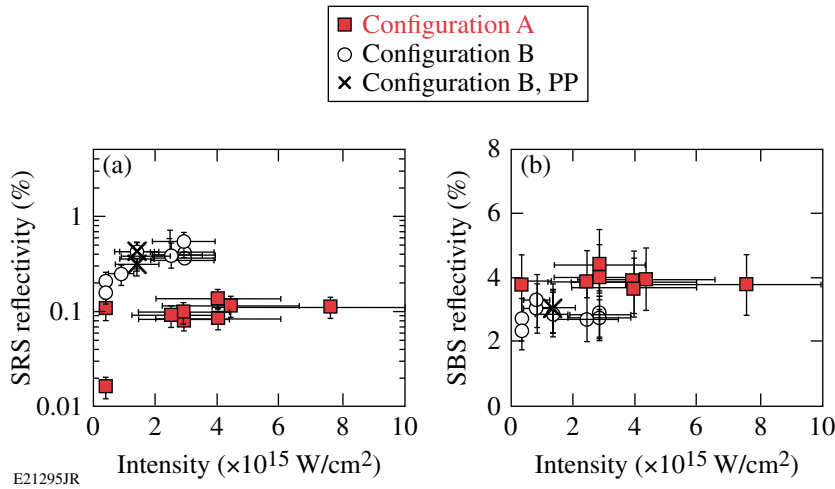


Figure 130.86

Percentage of reflected laser light in a drive beam port by (a) SRS and (b) SBS as a function of SBI. See Fig. 130.85 for an explanation of the different symbols.

uncertainty. In contrast to the experiment, collisional PIC simulations<sup>32</sup> for similar plasma conditions predict that the calculated reflected laser energy should remain constant at  $\sim 35\%$  when the laser intensity increases from  $1 \times 10^{15} \text{ W/cm}^2$  to  $8 \times 10^{15} \text{ W/cm}^2$ . The simulations show that the fraction of energy absorbed by the collisionless processes significantly increased with intensity, while the collisional absorption decreased proportionally.

A 2-D radiation–hydrodynamics code *DRACO*<sup>37</sup> simulation was performed to study the heating and profile modification of the plasma under the interaction of a single high-intensity ( $\sim 5 \times 10^{15} \text{ W/cm}^2$ ) spike beam with the imploding shell on the pole. The simulation shows the formation of a density depression in the underdense plasma and the steepening of the density profile at the critical density. Figure 130.87(a) shows axial density profiles for various times during the spike interaction.

Figure 130.87(b) shows the density scale length at the critical density  $n_c$  (circles) and at  $n_c/4$  (squares) along with the spike pulse’s profile (dashed). Profile steepening at  $n_c$  occurs during the spike interaction, and the density scale length is reduced from  $\sim 20 \mu\text{m}$  to  $\sim 2 \mu\text{m}$ . In contrast, the scale length at  $n_c/4$  does not change significantly and remains  $\sim 170 \mu\text{m}$  until the end of the spike pulse. As a result of this density profile modification, the spike pulse creates a channel through the underdense plasma. Scattered light is guided by this channel and is dominantly reflected back into the incident beam with very little sidescattering. This is supported by the small amount of scatter in the drive beam (Fig. 130.86) and the negligible amount of sidescattering shown by the near-backscatter diagnostic around the spike beam.

Time-resolved spectra of the SBS back-reflected light were recorded. Figure 130.88 shows two examples of the SBS sig-

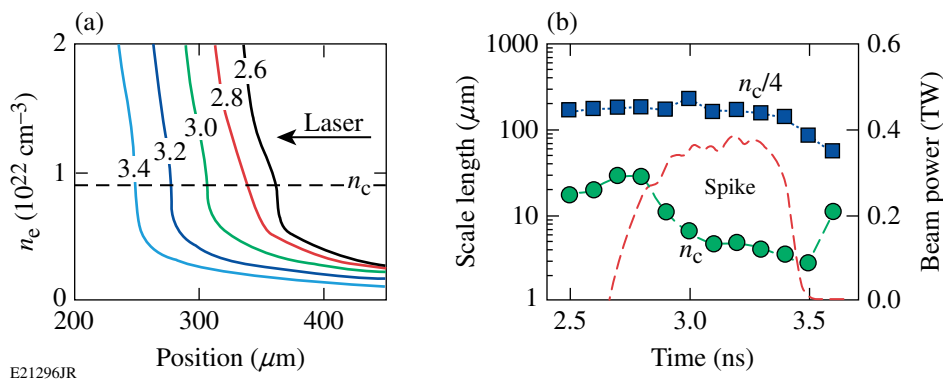


Figure 130.87

(a) Density profiles from a 2-D hydrodynamics code *DRACO*<sup>37</sup> simulation along the channel axis of a high-intensity spike beam interacting with the imploding shell. The numbers indicate the time in nanoseconds. The critical density is marked by the dashed line. (b) Density scale length at critical (circles) and quarter-critical (squares) density. Profile steepening occurs when the spike pulse (dashed) interacts.

nal for a medium- and high-intensity shot. The white curve represents the composite pulse shape of the drive and spike pulses. The SBS signal is produced only during the spike curve. The frequency spectrum of the SBS light is affected by the plasmas temperature and the Doppler shift with respect to the incident laser light. The amount of blue shift is given by  $\omega - \omega_0 = 2k_0c_s(M - 1)\sqrt{1 - n_e/n_c}$  (Ref. 38), where  $\omega$  and  $\omega_0$  are the angular frequencies of the scattered and incident light, respectively,  $k_0$  is the wave number of the incident light,  $c_s$  is the ion sound velocity, and  $M$  is the Mach number. Supersonic movement of the plasma region where SBS occurs will cause a blue shift of the SBS spectrum. The experiment shows that the blue shift is reduced with increasing laser intensity, indicating that SBS originates from plasma regions with lower flow velocities. A comparison with 2-D hydro simulations shows that lower flow velocities occur at higher plasma densities. The corresponding plasma density is indicated in Fig. 130.88 by the ratio of electron density to  $n_c$ . For an intensity of  $\sim 2.5 \times 10^{15} \text{ W/cm}^2$ , the SBS active region is located at a plasma density of  $\sim 0.03 n_c$ .

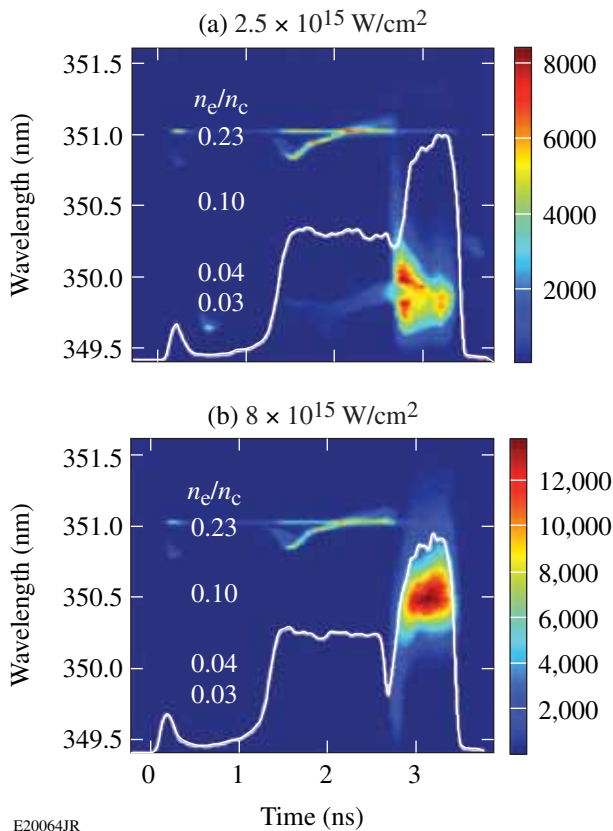


Figure 130.88  
Streaked SBS spectra for (a) medium ( $\text{SBI} = 2.5 \times 10^{15} \text{ W/cm}^2$ ) and (b) high ( $\text{SBI} = 8 \times 10^{15} \text{ W/cm}^2$ ) spike intensity. The numbers in the figures indicate the plasma density normalized to the critical density. The white curve is the composite pulse shape of the drive and spike pulses.

For  $\sim 4.5 \times 10^{15} \text{ W/cm}^2$  (not shown), the peak emission shifted to  $\sim 0.05 n_c$  with a weak SBS signal coming from up to  $\sim n_c/4$  later in time. At the highest intensity [Fig. 130.88(b)], the SBS active region shifts up to  $\sim 0.1$  to  $0.2 n_c$  with a clear indication of a signal coming from above  $n_c/4$ . The laser-intensity threshold for SBS can be estimated with

$$I_{\text{SBS}} \approx (T_{\text{keV}}/L_v \lambda_\mu) \times (n_c/n_e) \times 7 \times 10^{15} \text{ W/cm}^2 \text{ (Ref. 39),}$$

where  $T_{\text{keV}}$ ,  $L_v$ , and  $\lambda_\mu$  are the electron temperature in keV, scale length of the Mach number profile in microns, and the laser wavelength in microns, respectively. The resulting threshold is  $I_{\text{SBS}} \approx 5 \times 10^{14} \text{ W/cm}^2$  for the current plasma conditions and  $n_e/n_c = 0.04$ . The drive-pulse intensity is below the threshold, while the spike intensity is above the threshold.

The laser-intensity threshold for the TPD instability can be estimated from  $I_{\text{TPD}} \approx (82 \times T_{\text{keV}}/L_\mu \lambda_\mu) \times 10^{14} \text{ W/cm}^2$  (Ref. 40), where  $L_\mu$  is the density scale length in microns and  $\lambda_\mu$  is the laser wavelength in microns. For SRS, the threshold at around  $\sim n_c/4$  is given by

$$I_{\text{SRS}} \approx (T_{\text{keV}}/L_\mu^{4/3} \lambda_\mu^{2/3}) \times 5 \times 10^{16} \text{ W/cm}^2 \text{ (Ref. 39).}$$

*DRACO* simulations predict  $T_{\text{keV}} \approx 1.8$ , which results in  $I_{\text{TPD}} \approx 2.5 \times 10^{14} \text{ W/cm}^2$  and  $I_{\text{SRS}} \approx 2 \times 10^{14} \text{ W/cm}^2$  for the current plasma conditions. The thresholds are lower than the peak intensity in the drive beams, but no SRS or TPD signatures were measured with only the 40 drive beams. With increasing intensity, a strong reduction in the TPD instability is observed, which is evident by the reduction in optical emission at the half-harmonic ( $\omega/2$ ) of the laser wavelength. The  $\omega/2$  signal decreased by more than two orders of magnitude in the applied intensity range. At the maximum intensity, the  $\omega/2$  signal was below the detection threshold, indicating no significant contribution of TPD to the hot-electron production. This and the relatively low hot-electron temperature of  $\sim 30 \text{ keV}$  support the conjecture that SRS plays the dominant role in hot-electron production in these experiments. The strong reduction of TPD with intensity, together with the observed shift of the SBS active region to  $\sim n_c/4$ , might indicate that driven ion-acoustic waves at  $\sim n_c/4$  play a role in the reduction of TPD.

## Conclusions

Spherical shock-ignition experiments were performed on OMEGA by using a beam configuration that separates low-intensity compression beams and high-intensity spike beams.  $\text{D}_2$ -filled plastic shells were compressed on a low adiabat by 40 of the 60 OMEGA beams, and the remaining 20 spike beams

were delayed and tightly focused onto the imploding shell to deliver a late shock. This article studied the implosion performance with the new beam configuration and used the platform to measure hot-electron production and laser backscattering for laser intensities that are relevant for shock ignition. Two different beam-pointing configurations were used: one that used the standard pointing to target center and another in which the beams were repointed to improve target illumination uniformity. Significant improvement in areal density and neutron yield and a rounder core in x-ray images were observed for the repointed beam configuration. The coupling of high-intensity spike beam energy into the imploding capsule was studied in experiments and simulations. Implosions in the standard configuration show a correlation between the measured neutron yield and the hard x-ray signal, which suggests that the yield increase was partially due to hot electrons coupled into the compressing target. The spike beams mitigated the large beam illumination nonuniformities in this configuration, which led to the recovery of the neutron yield by a factor of  $\sim 14$ . Several indications suggest that when spike beams are equipped with phase plates, a stronger coupling of the spike beam energy into the imploding shell is achieved. With phase plates the following observations were made: lower backscatter losses, stronger x-ray emission in the 2- to 7-keV and  $>20$ -keV ranges, lower  $\rho R$ , and an earlier bang time. This indicates that higher coupling is achieved through increased thermal and hot-electron components. Two-dimensional hydrodynamic simulations were performed and show significant modulation in areal density. Similar modulations were observed in the experiments. Laser-plasma instabilities were studied for single-beam peak laser intensities of up to  $\sim 8 \times 10^{15}$  W/cm<sup>2</sup>, measuring backscattering of laser energy of up to 36% at the highest intensity. Hard x-ray measurements reveal a relatively low hot-electron temperature of  $\sim 30$  keV, which is independent of intensity and spike onset time. With increasing laser intensity, the region where stimulated Brillouin scattering occurs shifts to higher densities. At the highest intensity it occurs near and above the quarter-critical density. With higher intensity the two-plasmon-decay instability is suppressed and hot-electron production is dominated by stimulated Raman scattering.

These experiments measured a low hot-electron temperature, not too high backscatter losses, and a good coupling of spike beam energy into an imploding capsule at laser intensities of up to  $\sim 8 \times 10^{15}$  W/cm<sup>2</sup>, which is encouraging for the shock-ignition concept. A low hot-electron temperature is beneficial since these electrons are stopped in the outer layer of the imploding target, augmenting the strong hydrodynamic shock. Further shock-ignition experiments are required, however, to

study laser-plasma instabilities and hot-electron production at plasma conditions with longer density scale lengths and higher electron temperatures that are closer to those of an ignition design.

#### ACKNOWLEDGMENT

This work was supported by the U.S. Department of Energy Office of Fusion Energy Sciences under contract DE-FC02-04ER54789 and by the Office of Inertial Confinement Fusion under Cooperative Agreement No. DE-FC52-08NA28302, the University of Rochester, and the New York State Energy Research and Development Authority. The support of DOE does not constitute an endorsement by DOE of the views expressed in this article. This work was partially supported by the Aquitaine Region Council and the European Union's Seventh Framework Program: the HiPER project #211737.

#### REFERENCES

1. R. Betti, C. D. Zhou, K. S. Anderson, L. J. Perkins, W. Theobald, and A. A. Solodov, *Phys. Rev. Lett.* **98**, 155001 (2007).
2. R. L. McCrory, D. D. Meyerhofer, R. Betti, R. S. Craxton, J. A. Delettrez, D. H. Edgell, V. Yu Glebov, V. N. Goncharov, D. R. Harding, D. W. Jacobs-Perkins, J. P. Knauer, F. J. Marshall, P. W. McKenty, P. B. Radha, S. P. Regan, T. C. Sangster, W. Seka, R. W. Short, S. Skupsky, V. A. Smalyuk, J. M. Soures, C. Stoeckl, B. Yaakobi, D. Shvarts, J. A. Frenje, C. K. Li, R. D. Petrasso, and F. H. Séguin, *Phys. Plasmas* **15**, 055503 (2008).
3. J. D. Lindl, *Inertial Confinement Fusion: The Quest for Ignition and Energy Gain Using Indirect Drive* (Springer-Verlag, New York, 1998).
4. V. A. Shcherbakov, *Sov. J. Plasma Phys.* **9**, 240 (1983).
5. R. Betti and C. Zhou, *Phys. Plasmas* **12**, 110702 (2005).
6. X. Ribeyre *et al.*, *Plasma Phys. Control. Fusion* **50**, 025007 (2008).
7. A. J. Schmitt, J. W. Bates, S. P. Obenschain, S. T. Zalesak, D. E. Fyfe, and R. Betti, *Fusion Sci. Technol.* **56**, 377 (2009).
8. X. Ribeyre *et al.*, *Plasma Phys. Control. Fusion* **51**, 015013 (2009).
9. E. I. Moses *et al.*, *Phys. Plasmas* **16**, 041006 (2009).
10. L. J. Perkins, R. Betti, K. N. LaFortune, and W. H. Williams, *Phys. Rev. Lett.* **103**, 045004 (2009).
11. M. Dunne, *Nat. Phys.* **2**, 2 (2006); HiPER, accessed 7 May 2012, <http://www.hiper-laser.org/index.asp>.
12. W. L. Kruer, *The Physics of Laser-Plasma Interactions*, *Frontiers in Physics*, Vol. 73, edited by D. Pines (Addison-Wesley, Redwood City, CA, 1988).
13. R. Betti, W. Theobald, C. D. Zhou, K. S. Anderson, P. W. McKenty, S. Skupsky, D. Shvarts, V. N. Goncharov, J. A. Delettrez, P. B. Radha, T. C. Sangster, C. Stoeckl, and D. D. Meyerhofer, *J. Phys., Conf. Ser.* **112**, 022024 (2008).
14. J. Delettrez, R. Epstein, M. C. Richardson, P. A. Jaanimagi, and B. L. Henke, *Phys. Rev. A* **36**, 3926 (1987); M. C. Richardson, P. W. McKenty, F. J. Marshall, C. P. Verdon, J. M. Soures, R. L. McCrory, O. Barnouin,

- R. S. Craxton, J. Delettrez, R. L. Hutchison, P. A. Jaanimagi, R. Keck, T. Kessler, H. Kim, S. A. Letzring, D. M. Roback, W. Seka, S. Skupsky, B. Yaakobi, S. M. Lane, and S. Prussin, in *Laser Interaction and Related Plasma Phenomena*, edited by H. Hora and G. H. Miley (Plenum Publishing, New York, 1986), Vol. 7, pp. 421–448.
15. T. R. Boehly, D. L. Brown, R. S. Craxton, R. L. Keck, J. P. Knauer, J. H. Kelly, T. J. Kessler, S. A. Kumpan, S. J. Loucks, S. A. Letzring, F. J. Marshall, R. L. McCrory, S. F. B. Morse, W. Seka, J. M. Soures, and C. P. Verdon, *Opt. Commun.* **133**, 495 (1997).
  16. W. Theobald, K. S. Anderson, R. Betti, R. S. Craxton, J. A. Delettrez, J. A. Frenje, V. Yu. Glebov, O. V. Gotchev, J. H. Kelly, C. K. Li, A. J. Mackinnon, F. J. Marshall, R. L. McCrory, D. D. Meyerhofer, J. F. Myatt, P. A. Norreys, P. M. Nilson, P. K. Patel, R. D. Petrasso, P. B. Radha, C. Ren, T. C. Sangster, W. Seka, V. A. Smalyuk, A. A. Solodov, R. B. Stephens, C. Stoeckl, and B. Yaakobi, *Plasma Phys. Control. Fusion* **51**, 124052 (2009).
  17. R. S. Craxton, L. Tucker, T. Mo, K. S. Anderson, R. Betti, L. J. Perkins, G. P. Schurtz, X. Ribeyre, and C. A. Casner, *Bull. Am. Phys. Soc.* **55**, 26 (2010).
  18. W. Theobald, R. Betti, C. Stoeckl, K. S. Anderson, J. A. Delettrez, V. Yu. Glebov, V. N. Goncharov, F. J. Marshall, D. N. Maywar, R. L. McCrory, D. D. Meyerhofer, P. B. Radha, T. C. Sangster, W. Seka, D. Shvarts, V. A. Smalyuk, A. A. Solodov, B. Yaakobi, C. D. Zhou, J. A. Frenje, C. K. Li, F. H. Séguin, R. D. Petrasso, and L. J. Perkins, *Phys. Plasmas* **15**, 056306 (2008).
  19. F. J. Marshall, J. A. Delettrez, R. Epstein, R. Forties, R. L. Keck, J. H. Kelly, P. W. McKenty, S. P. Regan, and L. J. Waxer, *Phys. Plasmas* **11**, 251 (2004).
  20. Y. Lin, T. J. Kessler, and G. N. Lawrence, *Opt. Lett.* **21**, 1703 (1996).
  21. T. R. Boehly, V. A. Smalyuk, D. D. Meyerhofer, J. P. Knauer, D. K. Bradley, R. S. Craxton, M. J. Guardalben, S. Skupsky, and T. J. Kessler, *J. Appl. Phys.* **85**, 3444 (1999).
  22. P.-H. Maire *et al.*, *SIAM J. Sci. Comput.* **29**, 1781 (2007).
  23. S. P. Regan, T. C. Sangster, D. D. Meyerhofer, W. Seka, R. Epstein, S. J. Loucks, R. L. McCrory, C. Stoeckl, V. Yu. Glebov, O. S. Jones, D. A. Callahan, P. A. Amendt, N. B. Meezan, L. J. Suter, M. D. Rosen, O. L. Landen, E. L. DeWald, S. H. Glenzer, C. Sorce, S. Dixit, R. E. Turner, and B. MacGowan, *J. Phys., Conf. Ser.* **112**, 022077 (2008).
  24. C. D. Zhou, W. Theobald, R. Betti, P. B. Radha, V. A. Smalyuk, D. Shvarts, V. Yu. Glebov, C. Stoeckl, K. S. Anderson, D. D. Meyerhofer, T. C. Sangster, C. K. Li, R. D. Petrasso, J. A. Frenje, and F. H. Séguin, *Phys. Rev. Lett.* **98**, 025004 (2007).
  25. F. J. Marshall, T. Ohki, D. McInnis, Z. Ninkov, and J. Carbone, *Rev. Sci. Instrum.* **72**, 713 (2001).
  26. V. Yu. Glebov, D. D. Meyerhofer, C. Stoeckl, and J. D. Zuegel, *Rev. Sci. Instrum.* **72**, 824 (2001).
  27. R. A. Lerche, D. W. Phillion, and G. L. Tietbohl, *Rev. Sci. Instrum.* **66**, 933 (1995).
  28. W. Seka, D. H. Edgell, J. P. Knauer, J. F. Myatt, A. V. Maximov, R. W. Short, T. C. Sangster, C. Stoeckl, R. E. Bahr, R. S. Craxton, J. A. Delettrez, V. N. Goncharov, I. V. Igumenshchev, and D. Shvarts, *Phys. Plasmas* **15**, 056312 (2008).
  29. C. Stoeckl, V. Yu. Glebov, D. D. Meyerhofer, W. Seka, B. Yaakobi, R. P. J. Town, and J. D. Zuegel, *Rev. Sci. Instrum.* **72**, 1197 (2001).
  30. F. H. Séguin, J. A. Frenje, C. K. Li, D. G. Hicks, S. Kurebayashi, J. R. Rygg, B.-E. Schwartz, R. D. Petrasso, S. Roberts, J. M. Soures, D. D. Meyerhofer, T. C. Sangster, J. P. Knauer, C. Sorce, V. Yu. Glebov, C. Stoeckl, T. W. Phillips, R. J. Leeper, K. Fletcher, and S. Padalino, *Rev. Sci. Instrum.* **74**, 975 (2003).
  31. S. Atzeni and J. Meyer-ter-Vehn, *The Physics of Inertial Fusion: Beam Plasma Interaction, Hydrodynamics, Hot Dense Matter*, International Series of Monographs on Physics (Clarendon Press, Oxford, 2004), p. 225.
  32. O. Klimo *et al.*, *Phys. Plasmas* **18**, 082709 (2011).
  33. C. Stoeckl, R. E. Bahr, B. Yaakobi, W. Seka, S. P. Regan, R. S. Craxton, J. A. Delettrez, R. W. Short, J. Myatt, A. V. Maximov, and H. Baldis, *Phys. Rev. Lett.* **90**, 235002 (2003).
  34. C. Labaune *et al.*, *Phys. Fluids B* **4**, 2224 (1992).
  35. B. J. MacGowan *et al.*, *Phys. Plasmas* **3**, 2029 (1996).
  36. J. D. Moody *et al.*, *Phys. Rev. Lett.* **86**, 2810 (2001).
  37. P. B. Radha, T. J. B. Collins, J. A. Delettrez, Y. Elbaz, R. Epstein, V. Yu. Glebov, V. N. Goncharov, R. L. Keck, J. P. Knauer, J. A. Marozas, F. J. Marshall, R. L. McCrory, P. W. McKenty, D. D. Meyerhofer, S. P. Regan, T. C. Sangster, W. Seka, D. Shvarts, S. Skupsky, Y. Srebro, and C. Stoeckl, *Phys. Plasmas* **12**, 056307 (2005).
  38. T. P. Hughes, in *Laser-Plasma Interactions*, edited by R. A. Cairns and J. J. Sanderson (SUSSP Publications, Edinburgh, 1980), p. 44.
  39. H. A. Baldis, E. M. Campbell, and W. L. Kruer, in *Handbook of Plasma Physics*, edited by A. Rubenchik and S. Witkowski, Physics of Laser Plasma, edited by M. N. Rosenbluth and R. Z. Sagdeev (North-Holland, Amsterdam, 1991), Vol. 3, p. 377.
  40. A. Simon, R. W. Short, E. A. Williams, and T. Dewandre, *Phys. Fluids* **26**, 3107 (1983).